

Highly active single-layer 2H-MoS₂ for CO₂ hydrogenation to methanol

Shenghui Zhou^{a,b,c}, Wenrui Ma^a, Mohammadreza Kosari^{a,d}, Alvin M.H. Lim^{a,b}, Sergey M. Kozlov^{a,*}, Hua Chun Zeng^{a,b,**}

^a Department of Chemical and Biomolecular Engineering, College of Design and Engineering, National University of Singapore, Singapore 119260, Singapore

^b The Cambridge Centre for Advanced Research and Education, Singapore 1 CREATE Way, 138602, Singapore

^c School of Chemistry, Chemical Engineering and Biotechnology, Nanyang Technological University, 62 Nanyang Drive, 637459, Singapore

^d Chemical and Biomolecular Engineering Department, College of Engineering, North Carolina State University, 911 Partners Way, Raleigh, NC, USA

ARTICLE INFO

Keywords:

CO₂ hydrogenation

Methanol

Single-layer MoS₂

Density functional theory

Facile and scalable fabrication

ABSTRACT

Few-layer MoS₂ were recently discovered as promising catalyst for CO₂ hydrogenation to methanol, despite extreme conditions proposed for its synthesis. Herein, we developed an exceptionally facile, safe, and scalable strategy to prepare single-layer MoS₂ (s-MoS₂) at ambient pressure using instantaneous self-assembled micelles of didodecyltrimethylammonium (DA)-MoS₄ complexes as precursor. During the pyrolysis, the presence and subsequent decomposition of coordinated DA inhibited the growth and sheet-stacking of MoS₂ in *c*-direction, resulting in discrete s-MoS₂ molecular sheets which maximize the exposure of in-plane S vacancies (Sv). Remarkably, s-MoS₂ displayed 77% methanol selectivity and methanol space time yield of 1.54 g·g_{MoS₂}⁻¹·h⁻¹, representing the top levels among reported MoS₂ catalysts under similar conditions. Density functional theory (DFT) simulations attribute high activity of s-MoS₂ to its ability to stabilize in-plane low-coordinated Mo atoms in the vicinity of Sv on both sides of monolayer. The superior performance of s-MoS₂ creates new prospects for technological applications beyond CO₂ hydrogenation.

1. Introduction

The excessive emissions of anthropogenic CO₂ in the atmosphere have caused unprecedented climate and environmental crisis [1–6]. Catalytic hydrogenation of CO₂ with preferentially renewable hydrogen source to fabricate clean liquid fuels and valuable chemicals, commonly referred to as “liquid sunshine”, is recognized to be a sustainable and promising strategy. This approach aims to address the greenhouse effect and reduce humanity’s dependence on fossil fuels [7–9]. In particular, the synthesis of methanol from CO₂ has garnered significant interest because methanol is not only considered an alternative fuel but also serves as a versatile precursor that can be further transformed into light olefins, gasoline, or other high-value chemicals, aligning with the concept of “methanol economy” [10,11]. Over recent decades, substantial research endeavors have been directed towards the development of high-performance catalysts for CO₂ hydrogenation to methanol, including Cu-metal oxides (Cu/ZnO, [12,13] Cu/ZrO₂ [14]), In₂O₃-based oxide, [15–17] ZnO/ZrO₂-solid solution, [18] Co@SiO₂, [19]

metal alloys (AuZn, [20] NiGa, [21] PdCu [22]), Pd/Mo₂N, [23] Mo₂C, [24] MoS₂, [25] etc.

Among these catalysts, MoS₂ attracted significant attention because it worked at low reaction temperature with superior stability [25,26]. However, such few-layered MoS₂ required hydro-solvothermal synthesis in a specially designed airtight autoclave at high temperature and extremely high pressure and hazardous CS₂ as a sulfidation reagent, imposing synthetic burden and process risks [27]. Under these harsh reaction conditions, a custom-made pressure-resistant equipment was required [28]. Thus, such extreme preparative conditions may limit the industrial scale production and application of this catalyst. Notably, MoS₂ exhibits a more intricate structure compared to conventional metal oxide catalysts and its structure has a crucial effect on selective methanol synthesis, making it challenging to achieve high methanol yields in CO₂ hydrogenation. Namely, MoS₂ encompasses three phases (1 T, 2 H, and 3 R), diverse layered structures (multilayer, few-layer, and single-layer) and two categories of active sites (in-plane and edge sites) [29]. Conventionally synthesized MoS₂ had mostly multi-layer structure

* Corresponding author.

** Corresponding author at: Department of Chemical and Biomolecular Engineering, College of Design and Engineering, National University of Singapore, Singapore 119260, Singapore.

E-mail addresses: sergey.kozlov@nus.edu.sg (S.M. Kozlov), chezhc@nus.edu.sg (H.C. Zeng).

<https://doi.org/10.1016/j.apcatb.2024.123870>

Received 4 November 2023; Received in revised form 19 February 2024; Accepted 21 February 2024

Available online 23 February 2024

0926-3373/© 2024 Elsevier B.V. All rights reserved.

and thus exhibited poor performance for methanol synthesis due to limited dispersion [25]. The catalysis of methanol synthesis is primarily facilitated by the 2 H-phase MoS₂, specifically those instances with an adequate presence of in-plane sulfur vacancies (Sv). In contrast, MoS₂ featuring abundant edge Sv predominantly enhances methane production [25]. Based on these observations, one could expect that if multi-layer or few-layer MoS₂ transforms into single-layer MoS₂, the intermediate layers of MoS₂ can become fully exposed, thereby maximizing the generation of in-plane Sv. Besides, the active in-plane Sv of freestanding single-layer MoS₂ will be highly accessible, and thus effectively boost the performance of both sides of this molecular sheet for methanol synthesis. However, the current synthesis methods for single-layer MoS₂ are mainly the mechanical exfoliation by adhesive Scotch tape and chemical exfoliation by alkali metal intercalation (Figure S1) [30]. Undoubtedly, the mechanical exfoliation method poses challenges when it comes to scaling up for mass production. Besides, the determination of the location and layer number of mechanically exfoliated nanosheets is a time-intensive process [30]. Furthermore, the chemical exfoliation method is synthetically cumbersome, expensive, difficult to scale up and the materials are highly sensitive to operating conditions [31]. The elimination of reactive intercalators from the solution frequently results in the prompt re-aggregation of exfoliated layers and the generation of wastes (e.g. Li containing wastes and organic solvents) [31]. Moreover, the processes of intercalation and de-intercalation linked to electronic changes also prompt structural transformations, such as the transition from the 2 H to the 1 T phase, in MoS₂ [30]. Accordingly, albeit challenging, development of extremely mild, facile, scalable routes to synthesize discrete molecular sheets of 2 H-phase MoS₂ with abundant in-plane sites is highly desirable for efficient CO₂ hydrogenation to methanol.

In recent years, by using various cationic surfactants as templates, capping agent, or charge-balancing species, our group has conducted research on various hierarchical porous nanocatalysts to investigate unsolved challenges in established heterogeneous reactions through the strategic design of catalytic inorganic nanocomposites [32–34]. Encouraged by our previous research, herein, we report an exceptionally simple, safe, and scalable approach for synthesizing single-layer MoS₂ (s-MoS₂) under ambient pressure. Didodecyltrimethylammonium (DA) cations with two long-chain alkyl groups were used as counterions to fabricate DA₂–MoS₄ precursor under the condition of stirring for 30 s at

room temperature. During the mild thermal transformation, the presence and subsequent decomposition of long-chain DA inhibited the growing and stacking of MoS₂ sheets in the *c*-direction, leading to the formation of single-layer MoS₂ (s-MoS₂) with abundant pores (Fig. 1), which can effectively promote mass transfer and greatly maximize exposure and accessibility of active in-plane Sv. As expected, the obtained s-MoS₂ catalyst exhibited significantly outstanding performance and stability in CO₂ hydrogenation to methanol, which markedly surpassed commercial Cu/ZnO/Al₂O₃ and previously reported Mo-based catalysts in literature. More importantly, the catalysts were durable on stream and the synthesis of s-MoS₂ can be easily scaled up for mass production, fulfilling the basic requirements for industrial applications. Experimental findings, coupled with density functional theory (DFT) calculations, demonstrate that the single-layer MoS₂ exhibits higher CO₂ hydrogenation activity due to low-coordinated Mo atoms adjacent to S vacancies formed on opposite sides of MoS₂ monolayers.

2. Experimental section

2.1. Chemicals and materials

Didodecyltrimethylammonium bromide (DAB), ammonium heptamolybdate tetrahydrate ((NH₄)₆Mo₇O₂₄·4H₂O, >99%), ammonium tetrathiomolybdate ((NH₄)₂MoS₄, ATM, >99%), ammonium tetrathiotungstate ((NH₄)₂WS₄, >99%), thioacetamide (>99%) and commercial molybdenum disulfide (c-MoS₂, 99%, < 2 μm) were from Sigma-Aldrich. Commercial Cu/ZnO/Al₂O₃ catalyst were obtained from Alfa Aesar.

2.2. Synthesis of single-layer MoS₂ (s-MoS₂) and multilayer MoS₂ (m-MoS₂)

Briefly, 150 mg of ATM was dissolved in 20.0 mL of deionized water to form a transparent red solution. 500 mg of DAB was dissolved in 20.0 mL of deionized water to form a transparent clear solution. Then, the two solutions were immediately mixed and stirred for 30 s. After that, the red solids (DAMS) were formed instantaneously (Figure S1). After pouring out the liquid, the remaining solids were placed in the oven at 80 °C for 3 h. Finally, the acquired samples were subjected to calcination in an Ar atmosphere at 550 °C for 2 hours with a ramping

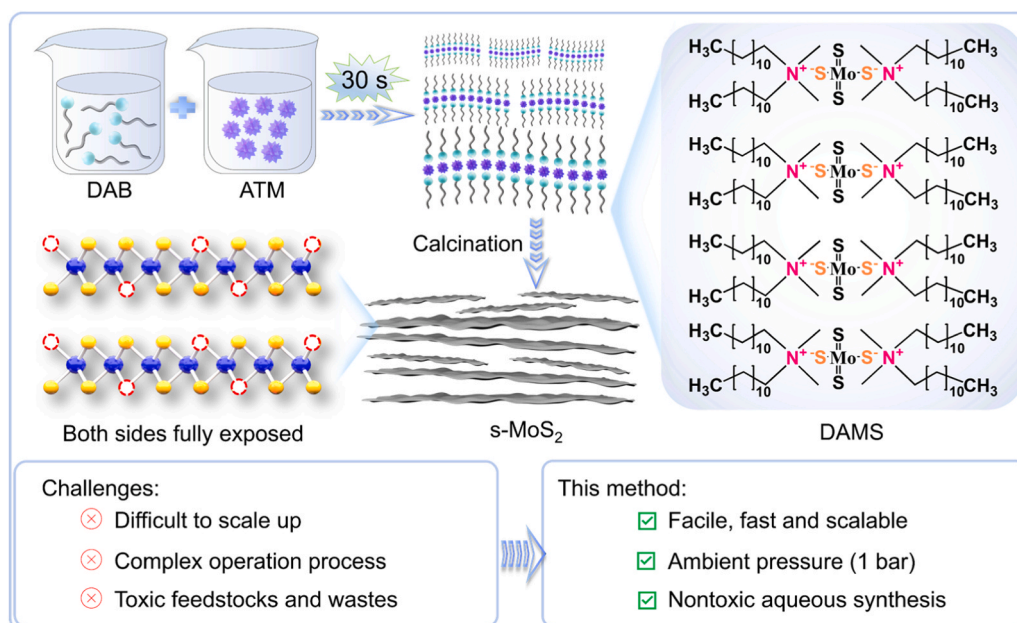


Fig. 1. Schematic illustration of the targeted synthesis of single-layer MoS₂ (s-MoS₂).

rate of 5 °C/min, resulting in the formation of the single-layer MoS₂ sample (s-MoS₂). The obtained single-layer MoS₂ has a monolithic aerogel structure. After sieving, the s-MoS₂ catalyst can be directly used for CO₂ hydrogenation test. For comparison, multilayer MoS₂ (m-MoS₂) can be obtained by direct calcining ATM under the same conditions.

2.3. Characterization methods

The catalysts were characterized using field-emission scanning electron microscopy (FESEM, JEOL-6700 F), transmission electron microscopy (TEM, JEM-2100), and high-resolution transmission electron microscopy (HRTEM, JEM-2100 F), Raman spectrometer (HORIBA Xplora Plus), X-ray diffraction (XRD, Bruker D8 Advance), inductively coupled plasma optical emission spectrometry (ICP-OES, Optima 7300DV, Perkin Elmer, USA), thermogravimetric analysis (TGA-2050, TA Instruments), N₂ adsorption/desorption (Quantachrome NOVA-3000 system), X-ray photoelectron spectroscopy (XPS, AXIS-HSi, Kratos Analytical, Al K_α, $h\nu = 1486.71$ eV), electron paramagnetic resonance spectroscopy (EPR, JES-FA), X-ray absorption spectroscopy (XAS). The detailed operating procedure is described in the [Supporting Information](#).

2.4. Hydrogenation of CO₂ in methanol synthesis

The catalytic activity measurements were conducted in a high-pressure fixed-bed flow reactor. Typically, 50 mg or 100 mg of the tested catalyst was loaded into the bottom of a quartz reaction tube with an inner diameter of 4 mm. The quartz tube was then enclosed in a stainless-steel reaction tube and sealed. An *in-situ* catalyst pretreatment was also performed under a constant flow of H₂ (20 mL/min) at 300 °C (ramp rate 10 °C/min) and 1 atm for 3 hours. After cooling to the desired reaction temperature, the feed mixture gas (H₂/CO₂ = 3/1 with 4% Ar as an internal standard, 20 mL/min) was introduced into the reaction tube. The composition of CO₂, H₂, and Ar (internal standard) was precisely controlled by a mass flow controller. The reactor was pressurized to 50 bar with a ramp rate of 2 bar/min. The outlet gas line was maintained at 453 K to prevent the condensation of gaseous products. Online sampling and analysis of the effluent were performed by an automated gas chromatography (GC, Agilent 8890 A) equipped with a thermal conductivity detector (TCD) and flame ionization detector (FID). The detailed process is described in the [Supporting Information](#).

2.5. DFT calculations

Spin-polarized density functional theory (DFT) calculations were performed using Vienna *Ab initio* Simulation Package (VASP) [35–37]. The Perdew-Burke-Ernzerhof (PBE) implementation of the generalized gradient approximation (GGA) was used as the exchange-correlation functional [38]. Valence electron orbitals of Mo (4s²4p⁶4d⁵5s¹), S (3s²3p⁴), C (2s²2p²), O (2s²2p⁴), and H (1s¹) were expended using plane-wave-basis set with a cut-off energy of 400 eV. The core-valence interaction was described by the projector augmented wave method [39,40]. The long-range van der Waals interactions were considered by applying the zero-damping DFT-D3 correction as implemented in VASP [41]. For all calculations, we sampled only the Γ point of the Brillouin zone. Electronic self-consistent loop was terminated when the energy change was below 1×10^{-5} eV. The convergence was accelerated by the 1st order Methfessel-Paxton smearing with a width of 0.1 eV [42]. Geometry optimizations were considered converged when the maximum force acting on the atoms dropped below 0.03 eV/Å. Vibrational analysis calculations were performed using the finite differences approach with a step width of ± 0.015 Å. Transition states were located using the nudge elastic band or dimer methods, and confirmed to have only one imaginary frequency [43,44]. We confirmed the corresponding initial and final states by obtaining the minimum energy pathway after disturbing and relaxing the transition state along the imaginary vibrational

mode.

Single-layer and double-layer 5×5 MoS₂ slabs with 16 Å vacuum in the z direction were used to simulate MoS₂ catalysts. The sulfur vacancy formation energy (E_{svf}) was defined as

$$E_{svf} = E(\text{Mo}_x\text{S}_{y-1}) + E(\text{H}_2\text{S}) - E(\text{Mo}_x\text{S}_y) - E(\text{H}_2)$$

where $E(\text{Mo}_x\text{S}_y)$ and $E(\text{Mo}_x\text{S}_{y-1})$ are the total energies of MoS₂ and MoS₂ with one more S vacancy, respectively. $E(\text{H}_2\text{S})$ and $E(\text{H}_2)$ represent the energies of an isolated H₂S and H₂ in the gas phase, respectively. Relative energy plotted on the reaction profile was calculated with reference to the sum of total energies of a clean MoS₂ slab, three isolated H₂ molecules, and one isolated CO₂ molecule. The Gibbs free energy (G) was obtained using the following equation:

$$G = E_{\text{DFT}} + \text{ZPVE} + H_{\text{vib}} - TS_{\text{vib}}$$

where E_{DFT} is the DFT total energy, while ZPVE, H_{vib} , and S_{vib} are the zero-point vibrational energy, enthalpy, and entropy calculated from the vibrational frequencies, respectively. We adopted the ideal gas approximation to get the Gibbs free energy of gas-phase molecules. The Gibbs free energy corrections for relative energy are calculated for the following reaction conditions: (T = 533 K, P(H₂) = 37.5 bar, P(CO₂) = 12.5 bar, P(CH₃OH) = 0.75 bar, P(H₂O) = 0.75 bar). In turn, the Gibbs free energy S vacancy formation energy is calculated for the reduction condition: T = 573 K, P(H₂) = 1 bar, P(H₂S) = 0.01 bar [45]. To describe the energetics of CO₂ reduction reaction, we apply an additional free energy correction of 0.44 eV to the gas phase CO₂, as suggested in previous studies [25,46].

3. Results and discussion

3.1. Synthesis and characterizations of catalysts

[Fig. 1](#) schematically illustrated the synthetic strategy for s-MoS₂, which mainly involved the instantaneous self-assembling and pyrolysis processes. First, a red suspended solids were obtained immediately after mixing the transparent didodecyldimethylammonium bromide (DAB) solution with the ammonium tetrathiomolybdate (ATM) solution ([Figure S2](#)). Subsequently, the as-assembled DA₂-MoS₄ (DAMS) precursor was converted to single-layer MoS₂ molecular sheet (s-MoS₂) via a mild calcination process at ambient pressure. For comparison, it was noted that ATM as a raw material could also be decomposed directly into MoS₂ through calcination, resulting in a multi-layered structure (referred to as m-MoS₂), without the instantaneous self-assembling processes [47].

Various techniques were employed to characterize the microstructure, composition, and morphology of the synthetic samples. Field-emission scanning electron microscopy (FESEM) images show the DAMS precursors are rough polymer structures with no pore structure ([Fig. S3](#)). After the heat treatment process, the as-obtained s-MoS₂ possesses abundant macropores of about 1–2 μm ([Figs. 2a](#) and [S4a-b](#)). In contrast, m-MoS₂ has a smooth surface and almost no pore structure ([Figs. 2b](#) and [S4c-d](#)). Furthermore, transmission electron microscopy (TEM) images show that s-MoS₂ also features large number of mesopores ([Fig. S4e](#)). A close inspection ([Fig. 2c](#)) reveals that s-MoS₂ is composed of monolayer sheets without stacking. To confirm that all the molecular sheets of MoS₂ in s-MoS₂ are freestanding, we randomly selected different locations in copper mesh to take high-resolution TEM (HRTEM) images. Our results show that all the MoS₂ in the HRTEM images are indeed single-layered, verifying the monolayer nature of s-MoS₂ catalysts ([Fig. S5](#)). On the contrary, TEM images ([Fig. 2d](#), [Figure S4f](#)) of m-MoS₂ display a typical layer-stacked structure (4–7 layers) with an interlayer spacing of ca. 6.3 Å, which is attributed to the lattice fringes of d_{002} of hexagonal MoS₂ (2 H-MoS₂; JCPDS No. 37–1492). To compare the performance of synthesized s-MoS₂ and m-MoS₂ with typical MoS₂-based catalysts, we also synthesized h-MoS₂

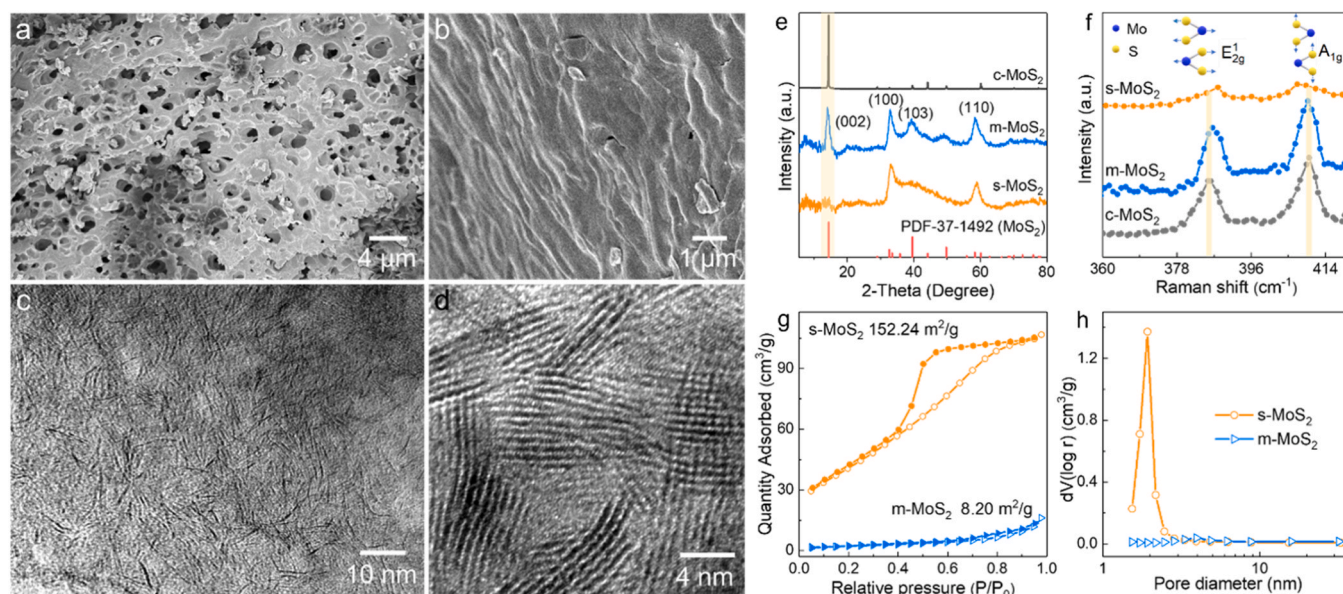


Fig. 2. Microscopy analysis and characterization of various as-prepared samples. FESEM of (a) s-MoS₂ and (b) m-MoS₂. HRTEM image of (c) s-MoS₂ and (d) m-MoS₂. (e) XRD patterns, (f) Raman spectra, (g) Nitrogen sorption isotherms, and (h) the corresponding pore-size distribution of the studied samples.

with flower-like multilayered structure (~ 10 layers). The synthetic process involved the application of the conventional hydrothermal method, employing ammonium heptamolybdate as the source of molybdenum (Mo) and thioacetamide as the sulfur source (Figure S6) [48]. In addition, the commercial MoS₂ powder (c-MoS₂) was composed of aggregated MoS₂ crystals ranging from 300 to 400 nm (Figure S7) with only small amounts of stacked sheet-like morphology visible.

The X-ray diffraction (XRD) analysis was carried out to explore the crystallinity and determine number of stacking layers of synthetic MoS₂ samples. As shown in Fig. 2e, all diffraction peaks at $2\theta = 14.0^\circ$, 33.0° , 39.2° , and 58.18° are in excellent agreement with the (002), (101), (103), and (110) reflections of 2 H-MoS₂, as indicated by the corresponding Powder Diffraction File (PDF) card No. 37-1492. Apparently, the (002) reflection peak of our s-MoS₂ appears to be unidentifiable in comparison with the XRD pattern of c-MoS₂, suggesting there is almost no layer-stacking of MoS₂ along the *c*-direction [49]. In contrast, the m-MoS₂ sample obtained by direct ATM calcination has an obvious (002) peak, which indicated that it has a multilayer structure. The XRD pattern of h-MoS₂ (Figure S8) shows that the (002) reflection was also distinct, suggesting that MoS₂ layers in h-MoS₂ are also highly stacked.

Raman spectroscopy test was further conducted to elucidate the structural features of these samples. As illustrated in Fig. 2f, all samples exhibit two characteristic MoS₂ Raman shifts at around 385.6 and 410.1 cm⁻¹, corresponding to the in-plane Mo-S phonon mode (E_{2g}^1), the out-of-plane Mo-S mode (A_{1g}), respectively [50]. Strikingly, we found that E_{2g}^1 vibration softened (red shifted), while the A_{1g} vibration evidently stiffened (blue shifts) in s-MoS₂ sample when compared with m-MoS₂ and c-MoS₂. This observation further validated the single-layer structure of s-MoS₂ as well as the multilayer structure of m-MoS₂, consistent with previous reports [51].

The pore characters and specific surface areas of various samples were examined by N₂ adsorption/desorption experiments at 77 K. As depicted in Fig. 2g, N₂ physisorption isotherms suggest that s-MoS₂ exhibit typical type-IV curves and an apparent characteristic H3-type hysteresis loop in $0.4 < P/P_0 < 1.0$, manifesting the presence of abundant mesoporous structures in s-MoS₂, which is also validated by the corresponding pore size distribution curves on the basis of Barrett-Joyner-Halenda (BJH) method (Fig. 2h). The Brunauer-Emmett-Teller (BET) specific surface areas of s-MoS₂ is determined to be 152.24 m²·g⁻¹. In contrast, m-MoS₂ and c-MoS₂ show negligible pore

structure with extremely low BET specific surface areas of only 8.2 and 2.4 m²·g⁻¹, respectively (Figure S9). This suggests that the presence and subsequent decomposition of DA in the precursor could promote the formation of porous structure in s-MoS₂.

The chemical compositions and states of various samples were examined by X-ray photoelectron spectroscopy (XPS). The survey spectrum in Figure S10a confirm the existence of Mo, S, and C elements in s-MoS₂. In the Mo 3d spectrum, two discernible peaks at 229.6 and 232.7 eV are evident, aligning with the binding energies of Mo 3d_{5/2} and Mo 3d_{3/2}, respectively (see Fig. 3a, Figure S10b). This observation indicates that the chemical state of Mo in both s-MoS₂ and m-MoS₂ is in the +4 state. The weak Mo⁶⁺ component is due to the oxidation in laboratory air during our sample preparation. Figure S10c depicts the S 2p spectra with two distinctive peaks at 162.5 eV for S 2p_{3/2} and 163.5 eV for S 2p_{1/2}, aligning with the binding energy of S²⁻ ions in both s-MoS₂ and m-MoS₂. Moreover, the presence of carbon residues in the s-MoS₂ has also been verified as the existence of C 1 s XPS spectra. Figure S10d shows S/Mo atomic ratios of s-MoS₂ decrease most distinctly among all catalysts, indicating the generation of abundant Sv in s-MoS₂ after reduction. In addition, the content of residual carbon was further measured (*ca.* 30.5 wt%) by thermogravimetric analysis (TGA, Figure S11).

Moreover, electron paramagnetic resonance (EPR) was employed to measure and compare the Sv number in different catalysts, as illustrated in Fig. 3b. Generally, the EPR test can detect the paramagnetic signals. The signal at around 330 mT ($g = 2.0$) probes into the concentration of unsaturated sites, which is positively correlated with the number of Sv in samples [52]. Apparently, s-MoS₂ exhibit a distinctly higher peak intensity than the c-MoS₂, h-MoS₂ and m-MoS₂. This suggested that a highly dispersed single-layer structure of s-MoS₂ could significantly promote the production and exposure of notably more Sv compared to multi-layer stacked m-MoS₂, h-MoS₂ and c-MoS₂.

The X-ray absorption near-edge structure (XANES) and extended X-ray absorption fine structure (EXAFS) were employed to probe the fine structures and coordination environment of Mo and S in different samples. Fig. 3c displays the Mo K-edge XANES spectra of s-MoS₂ and standard samples (Mo foil, MoO₃ and 2 H-MoS₂). The enlarged Mo K-edge XANES curves reveal that Mo foil possesses the smallest energy of absorption edge. The near-edge absorption energy of s-MoS₂ shifts to a lower value compared with 2 H-MoS₂, suggesting the lower Mo valence

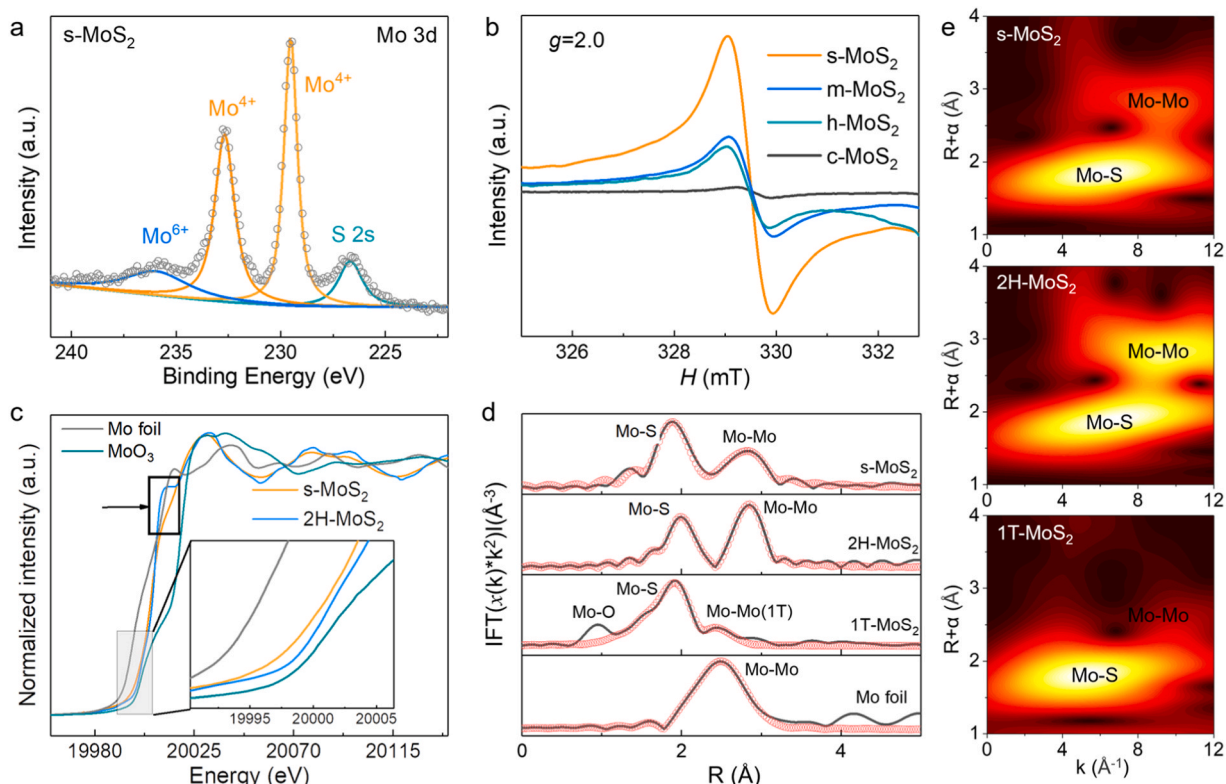


Fig. 3. Structure and physical property of catalysts. (a) Mo 3d high-resolution XPS spectra and (b) EPR spectra of various samples. (c) Mo K-edge XANES spectra, (d) FT-EXAFS curves and corresponding fits at the Mo K-edge, and (e) WT-EXAFS of various samples.

state and the presence of Sv in s-MoS₂. Furthermore, in comparison with 2 H-MoS₂, the absence of the characteristic feature at around 200.11 eV can be attributed to the erosion of the MoS₂ basal plane in s-MoS₂, providing additional confirmation of the defective MoS₂ lamellate structure. The Fourier-transformed extended X-ray adsorption fine structure (FT-EXAFS) at the Mo K-edge (Fig. 3d) indicates that s-MoS₂ and 2 H-MoS₂ exhibit two peaks at 1.9 and 2.5 Å, primarily arising from the scattering of the first shell Mo-S and the second shell Mo-Mo coordination. Subsequent quantitative EXAFS fitting was carried out to unveil detailed structural parameters. The comprehensive fitting results clearly indicate that the coordination number for the Mo-S shells in standard 2 H-MoS₂ and s-MoS₂ is 6 and 4.8, respectively (see Figure S12; Table S1). This outcome unequivocally demonstrates that the removal of sulfur from the MoS₂ basal plane significantly reduces the average coordination number of the Mo atoms. In addition, the coordination number of Mo-Mo shell in s-MoS₂ is also smaller than the theoretical values six, implying the excellent dispersion of the as-prepared single-layer MoS₂. Moreover, it can be seen that the second peak (Mo-Mo bond) of 1 T-MoS₂ downshifts from 2.9 to 2.5 Å and the peak intensity is inconspicuous. This distinction can be attributed to the octahedral coordination of Mo in 1 T-phase MoS₂ to relatively large sulfur scatterers, in contrast to the trigonal-prismatic coordination observed in 2H-MoS₂[53]. The evident structural evolution can be distinctly unveiled through the wavelet transform (WT) of Mo K-edge EXAFS oscillation. This technique visually displays the coordination structures of Mo, benefiting from its high resolution in both K and R spaces, as depicted in Fig. 3e.

Overall, combining the above characterizations we can conclude that the instantaneous self-assembly process of DAB and ATM was essential for the subsequent generation of the highly dispersed single-layer molecular sheets of MoS₂ with abundant Sv. The presence and subsequent decomposition of long-chain DA suppress the growing and stacking of MoS₂ sheets in the *c*-direction during thermal transformation, leading to

the formation of monolayer MoS₂ with abundant macropores and mesopores. In contrast, direct calcination of ATM only yielded a multi-layer stacked MoS₂ sheets with few pores. The monolayer dispersion and hierarchical porous structure of s-MoS₂ would be extremely favorable for the generation and maximization of exposed active Sv on both sides of molecular sheet (Fig. 3b).

3.2. Comparison of catalytic performance

The as-prepared various MoS₂-based catalysts (s-MoS₂, m-MoS₂ and h-MoS₂) as well as c-MoS₂ were evaluated for CO₂ hydrogenation to methanol. In this catalytic reaction, the main product is CH₃OH, while the side products are CO and CH₄ (Fig. 4a, b). Among these catalysts, bulk c-MoS₂ only provide 2.25% CO₂ conversion and 51.9% methanol selectivity at 260 °C. h-MoS₂ and m-MoS₂ also show unsatisfactory CO₂ conversion (< 8%) and methanol selectivity (< 52%) with low STY_{MeOH} (0.15 and 0.24 g_{cat}⁻¹·h⁻¹, respectively) at 260 °C. In contrast, the as-fabricated s-MoS₂ show significantly better CO₂ conversion and methanol selectivity than h-MoS₂, m-MoS₂ and c-MoS₂ over 180–260 °C. Under our optimal reaction conditions, s-MoS₂ catalyst can achieve a STY_{MeOH} yield up to 0.63 g_{cat}⁻¹·h⁻¹ with 12.16% CO₂ conversion and 63.4% methanol selectivity at 260 °C and GHSV of 24000 mL_{cat}⁻¹·h⁻¹. Regarding the catalytic hydrogenation of CO₂ to methanol over MoS₂-based catalysts, the catalytic performance is mainly positively related to the number of exposed Sv. Therefore, the MoS₂ catalysts with higher density of in-plane Sv and fewer layers of MoS₂ sheets are expected to obtain higher methanol yield. In our catalytic system, benefiting from the DAB assisted synthesis strategy, the prepared MoS₂ catalysts have highly dispersed single-layer molecular sheet structure. Because the formation and exposure of high-density Sv in s-MoS₂ can be maximized (ESR results from Fig. 3b), such highly exposed in-plane Sv are exceptionally advantageous for the selective production of methanol. Besides, H₂ pretreatment is necessary for high performance of MoS₂ catalysts

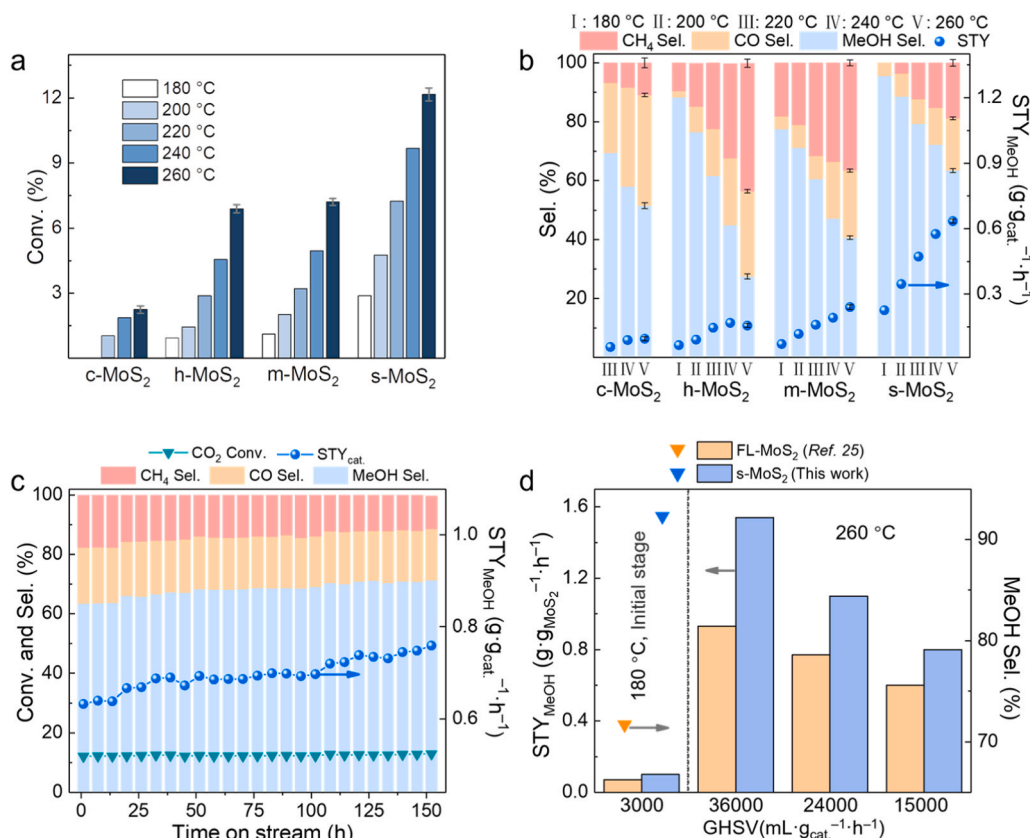


Fig. 4. Catalytic performance evaluation. (a) Conversion, (b) selectivity and STY_{MeOH} for CO_2 hydrogenation of different MoS_2 catalysts. (c) Long-term test of s- MoS_2 . Standard reaction conditions: 260 °C, 5 MPa, $CO_2:H_2 = 1:3$, $GHSV = 24000 \text{ mL} \cdot \text{g}_{\text{cat}}^{-1} \cdot \text{h}^{-1}$. (d) The comparison of the MeOH selectivity and STY_{MeOH} between s- MoS_2 and FL- MoS_2 in literature.

(Figure S13). To guarantee the reproducibility of this developed approach and the reliability of the hydrogenation reaction setting, we synthesized four different batches of s- MoS_2 catalysts repeatedly and evaluated their performance. The results show that the activity of all the catalysts are almost identical (Figure S13). Therefore, we conclude that the preparation and performance evaluation of s- MoS_2 catalyst are reliable and reproducible. Besides, we have also analyzed the effects of different reduction temperatures on reaction performance (Figure S14). We observed a significant decrease in CO_2 conversion with lower reduction temperatures, while a slight increase in CO_2 conversion was noted with higher reduction temperatures. Additionally, we found that the impact of reduction temperature on methanol selectivity is relatively minor. This suggests that a sufficiently high reduction temperature is necessary to promote the generation of sulfur vacancies.

Furthermore, we carried out a long-term stability test of s- MoS_2 at 260 °C for more than 150 h. As depicted in Fig. 4c, the CO_2 conversion and CH_3OH selectivity over s- MoS_2 catalysts exhibit a relatively rapid increase in the initial stage and then continue to increase slowly in the later stage of the hydrogenation process, indicating that the presence of reductive H_2 in reaction gas can lead to the formation of a higher concentration of Sv. This interpretation is supported by higher EPR response of used catalysts compared to pretreated fresh s- MoS_2 (Figure S15a). In turn, Figure S15b shows that S/Mo atomic ratios of used s- MoS_2 decreased notably, suggesting the removal of S and the generation of more Sv in s- MoS_2 after long-term reaction. When the long-term reaction time on stream is extended to 150 h, there are no any sign of decline in either CO_2 conversion, CH_3OH selectivity or STY_{MeOH} , validating the excellent stability of s- MoS_2 and its significant potential for industrial application. The XRD patterns and XPS spectra of recovered samples (Figure S15c-d) suggest the characteristic peaks of MoS_2 phase are nearly identical to the fresh MoS_2 catalysts indicate that the

characteristic peaks of the MoS_2 phase are nearly identical to those of the fresh catalysts. The recovered s- MoS_2 after the stability experiment is further studied by SEM and HRTEM (Figure S15e-f) techniques. The result shows that porous structure and highly dispersed single-layered MoS_2 nanosheets is well preserved after the stability tests. It is thus evident that the structure of s- MoS_2 was robust.

Afterwards, the effect of GHSV was investigated at 260 °C (Figure S16). The CO_2 conversion exhibited a decrease with the increase of GHSV while both the CH_3OH selectivity and STY_{MeOH} increased gradually. We can get higher STY_{MeOH} of $1.33 \text{ g} \cdot \text{g}_{\text{cat}}^{-1} \cdot \text{h}^{-1}$ and CH_3OH selectivity of 81.25% under high GHSV of $48000 \text{ mL} \cdot \text{g}_{\text{cat}}^{-1} \cdot \text{h}^{-1}$. This indicates that the over-hydrogenation of CO_2 to methanol is restricted at high GHSV and a short catalyst contact time can effectively suppress the formation of methane. We evaluated our s- MoS_2 under the same reaction conditions with previously reported FL- MoS_2 catalysts (Fig. 4d). Although the MoS_2 content of our catalyst is only 70% (100% MoS_2 content in FL- MoS_2 , Table S3), we still obtained higher STY_{MeOH} than FL- MoS_2 based on either per gram of catalyst or per gram of MoS_2 at same reaction temperature and GHSV. The initial selectivity (92.3%) of our catalyst at 180 °C is notably higher than that of FL- MoS_2 (71.7%), as FL- MoS_2 requires an extended induction period (about 300 h) for its selectivity to gradually reach satisfactory levels (Fig. 4d). In addition, the STY_{MeOH} value ($0.77 \text{ g} \cdot \text{g}_{\text{cat}}^{-1} \cdot \text{h}^{-1}$ at GHSV of $24000 \text{ mL} \cdot \text{g}_{\text{cat}}^{-1} \cdot \text{h}^{-1}$) obtained over our s- MoS_2 catalyst is also higher than those well-known catalysts (In_2O_3 , $In_2O_3/m-ZrO_2$, and ZnO/ZrO_2) from literature under similar or milder reaction conditions (Figure S17 and Table S2). Since the active metal content in each catalyst varies greatly (Table S3), we also use specific MeOH yield to fairly compare the activity of different catalysts. As shown in Table S2, the obtained specific MeOH yield ($5.5 \text{ mol} \cdot \text{mol}_{\text{Mo}}^{-1} \cdot \text{h}^{-1}$) and methanol selectivity (71.9%) over s- MoS_2 under a GHSV of $24000 \text{ mL} \cdot \text{g}_{\text{cat}}^{-1} \cdot \text{h}^{-1}$ at reaction temperature of 260 °C

after long-term stability test is also higher than other recently reported Mo, Cu or Pd-based catalysts in methanol synthesis reaction from CO₂ hydrogenation. It must be mentioned that the CO₂ conversion, MeOH selectivity and STY_{MeOH} strongly depend on the reaction temperature, GHSV, the ratio of H₂/CO₂ and the content of CO₂ in reaction gas. Besides, the addition of precious metals usually increases the activity of the catalyst significantly. Therefore, it is only reasonable to compare the catalytic performance of different catalysts without noble metal doping under the same GHSV and reaction gas composition. Furthermore, considering that with the extension of on-line long-term testing time, the activity of s-MoS₂ catalyst is still gradually increasing, we infer that the final conversion and selectivity would be higher by extending to longer reaction time based on the conclusion of previous literature [25]. More importantly, when compared to the previous high-pressure hydro-solvothermal method for the synthesis of few-layer MoS₂ at > 600 bar and 400 °C (Figure S18), our developed preparation process under ambient pressure is exceptionally simple, mild, rapid and does not require special equipment and highly toxic sulfidation reagents. Finally, it is worth mentioning that catalysts for industrial applications usually have granular structures after pelletizing. After calcining the DAMS precursors, the obtained s-MoS₂ in this work feature self-forming monolithic structure. Thus, when compared with FL-MoS₂ and Cu/ZnO/Al₂O₃, the synthesis of s-MoS₂ does not require an extrusion and forming step and can be directly used for industrial CO₂ hydrogenation (Figure S19). Overall, our monolithic single-layered MoS₂ catalysts have remarkable advantages in low process requirement but high catalytic performance, and therefore hold great promise for industrial applications of CO₂ hydrogenation to methanol.

3.3. Scale-up and generality of synthesis strategy

As the s-MoS₂ was extremely facile to prepare, the catalyst could be

easily scaled up for large scale production in the laboratory. By simply regulating the fabrication parameters in equal proportions, this developed synthetic protocol was readily scaled up 50-fold to achieve gram-scale synthesis of s-MoS₂ (Fig. 5a). The HRTEM image shows that s-MoS₂ in a large quantity also exhibited a highly dispersed monolayer sheet-like structure (Fig. 5b). More importantly, there is negligible variance in catalytic performance when compared to the samples produced on a smaller scale. (Fig. 5c). This result validates the huge potential of this approach for widespread implementation in industrial-scale production. To explore the generality of this synthetic strategy, ATM was replaced with (NH₄)₂WS₄ for the preparation of single-layer WS₂. As anticipated, HRTEM images (Fig. 5d) affirmed that the (DA)₂WS₄ precursors can also be converted into the corresponding single-layered WS₂ sheets. Hence, we reveal that the feasibility and versatility of the developed synthetic approach of s-MoS₂ would inspire the future development of other single-layered transition-metal dichalcogenides.

3.4. Mechanistic investigation of CO₂ hydrogenation

We initially employed temperature-programmed surface reaction (TPSR) coupled with mass spectrometry (MS) to investigate the formation of Sv by H₂ treatment and the subsequent reaction process. As illustrated in Fig. 6a, signals corresponding to SO₂, H₂O, and H₂S were directly observed during the reduction process, signifying the elimination of O atoms and certain S atoms from MoS₂ through H₂ pretreatment. The O atoms might originate from the oxidation of MoS₂ during the synthesis process or when the material is exposed to air. This reaffirms that the reduction of S by H₂ results in the creation of Sv and the exposure of coordinatively unsaturated Mo atoms. It is noteworthy that the initial temperature of H₂S and SO₂ production is significantly lower for s-MoS₂ than for m-MoS₂, and the peak height of H₂S is also

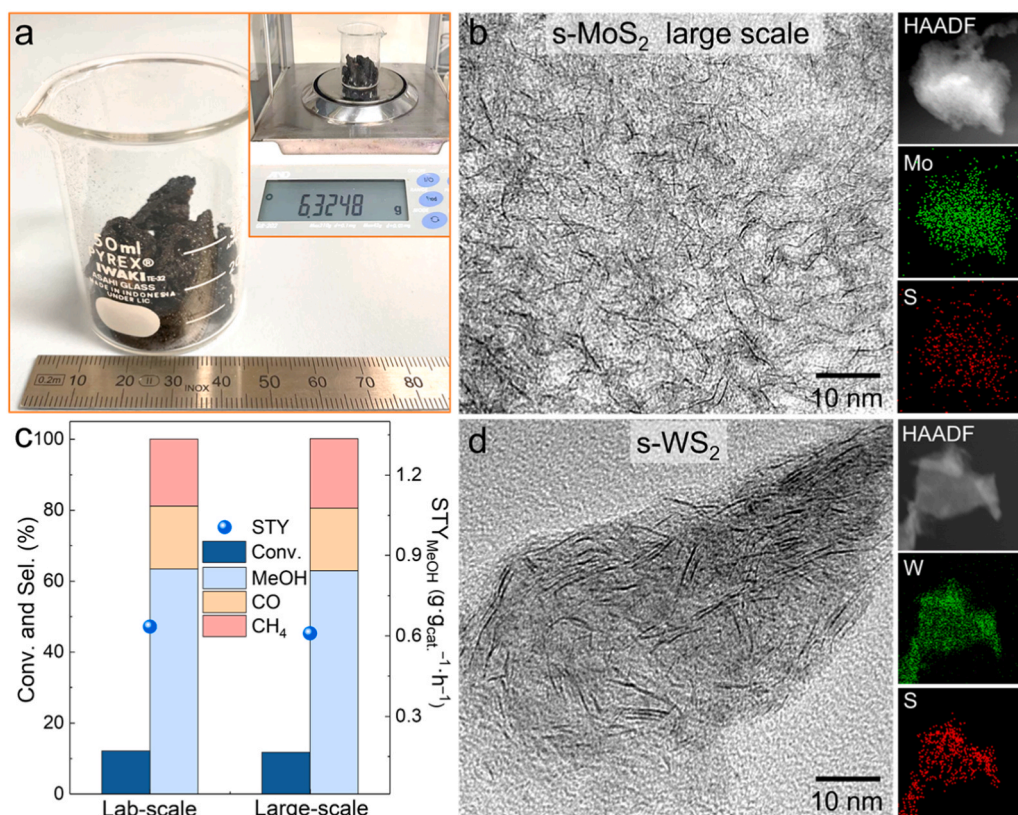


Fig. 5. Scale-up preparation and versatility of the developed approach. (a) Photographs of s-MoS₂ synthesized on a larger scale in a single batch. (b) HRTEM images of large-scale s-MoS₂. (c) Evaluation of the catalytic performance of catalysts synthesized at varying scales. (d) HRTEM images of s-WS₂.

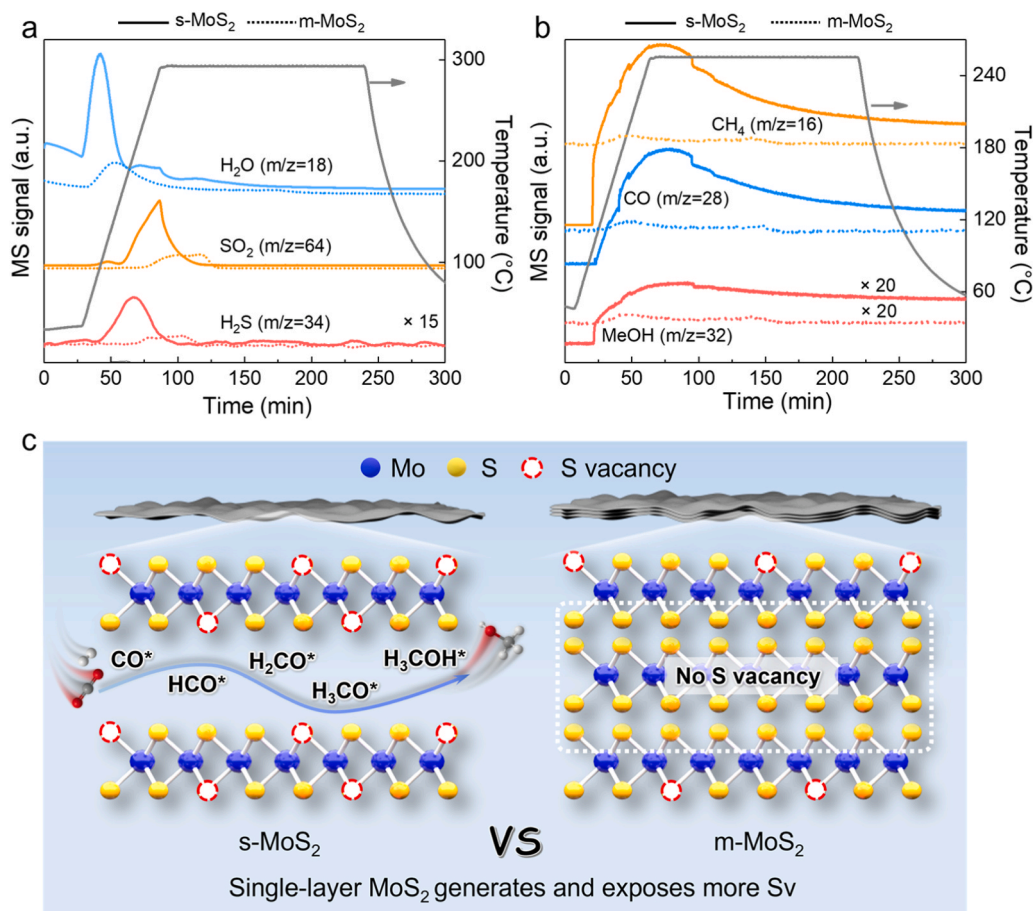


Fig. 6. TPSR over s-MoS₂ and m-MoS₂ based on the (a) H₂ pretreatment process and (b) CO₂ hydrogenation reaction. (c) Reaction mechanism for CO₂ hydrogenation over s-MoS₂ and the comparison on the exposure of sulfur vacancies between s-MoS₂ and m-MoS₂.

significantly higher for s-MoS₂ than for m-MoS₂. This indicates that monolayer MoS₂ is more susceptible to H₂ reduction to create more Sv than multilayer MoS₂. Following the pre-activation of the MoS₂ samples, CO₂ gas was introduced into the reactor at 50 °C for 60 minutes to facilitate CO₂ chemisorption and activation on the sample surface. Then, H₂ was introduced and the temperature was increased to 260 °C. The production was immediately observed with the increasing signal for s-MoS₂ and m-MoS₂ samples (Fig. 6b). Importantly, the increase of production signal (CO, CH₄, and CH₃OH) over s-MoS₂ occurs at around 100 °C while production begins to form at ~200 °C over m-MoS₂. This indicates the superior activation of CO₂ on the surface of s-MoS₂.

In order to detect the reaction intermediates and accordingly investigate the catalytic reaction mechanism, we firstly carried out high pressure *in situ* DRIFTS experiments at 240 °C and 30 bar with s-MoS₂ and m-MoS₂. As shown in Figure S20-S21, *in situ* DRIFTS spectra were collected during CO₂ hydrogenation using s-MoS₂ and m-MoS₂ catalysts, respectively. Upon the introduction of the reaction gas, the gradually increasing absorption peaks at ~2077 cm⁻¹, 910–970 cm⁻¹ and 760–800 cm⁻¹ can be assigned to the linearly bridged CO* species, the Mo=O species and the Mo–O–Mo species. This indicates that coordinatively unsaturated Mo in s-MoS₂ can easily dissociate CO₂ to *O and *CO species on active edge Sv and in plane Sv [25,54–56]. It is noteworthy that the generation of *CO species could also potentially arise from the hydrogenation of CO₂, leading to the production of CO. The obvious broad bands at 2177 and 2113 cm⁻¹ are assigned to gaseous CO, suggesting the presence of RWGS side reaction [57]. The bands at 2780–3000 cm⁻¹ can be ascribed to the ν(CH₃) modes of the methoxy species [25,58]. Moreover, the bands at 1054, 1031, and 1007 cm⁻¹ attributed to the C–O stretching of CH₃OH are also identified,

confirming the formation of methanol [57]. Additionally, the absorbance peak located at 3014 cm⁻¹ can be ascribed to CH₄. The bands at 3014, 2928, 2077 and 1054 cm⁻¹ are chosen to study the dynamic changes of CH₄, CH₃O*, CO* and CH₃OH at 240 °C. The peak intensity of all these species increases with prolongation of reaction time, implying the progressive generation and enrichment of each surface species with increased reaction time. For comparison, *in situ* DRIFTS experiments were also performed over m-MoS₂ (Figure S21). The results indicate that m-MoS₂ also exhibits similar bands, suggesting the presence of the same intermediates and a comparable transformation pathway of CO₂ to methanol over m-MoS₂. However, the intensity of all the peaks in m-MoS₂ is significantly weaker than those in s-MoS₂, further underscoring the inferior catalytic activity of m-MoS₂. Subsequently, we carried out *in situ* DRIFTS study under a gas flow of CO₂/H₂ and pure H₂ at 240 °C and ambient pressure to investigate dynamic evolution of different species. As the reaction proceeded, all the characteristic peaks grow up. When switching CO₂/H₂ to H₂, the CO* intermediates, Mo=O and Mo–O–Mo species almost disappeared, while the CH₃O* and CH₃OH decreased slowly. This indicates that the constant transformation of CO* to CH₃O* and CH₃OH. Based on the characterization of catalysts, *in situ* DRIFTS test and previous research advances, [25] we validate a plausible catalytic mechanism for methanol production from CO₂ hydrogenation over s-MoS₂. As depicted in Fig. 6c, initially, CO₂ could be adsorbed on active in-plane Sv of s-MoS₂ and readily dissociated to CO* and O* species. Next, CO* species were hydrogenated step by step to generate CHO*, CH₂O* and CH₃O* intermediates, and eventually to produce CH₃OH [25]. Illustratively, Fig. 6c also demonstrates that single layered MoS₂, due to its bilaterally exposed nature, can significantly expose more Sv, enhancing its catalytic properties, while multiple-layer MoS₂

can only partially expose the active Sv on either side of the m-MoS₂ layer stacks. Clearly, Sv cannot be generated or be accessible effectively in the intermediate layer(s) of m-MoS₂. This further reveals the distinct advantage of s-MoS₂ in CO₂ hydrogenation to methanol.

3.5. Theoretical insight into the effect of thickness of MoS₂ on CO₂ hydrogenation to methanol

We utilized DFT calculations to reveal the reason for higher catalytic performance of single-layer MoS₂ over multi-layer MoS₂ in CO₂ reduction to methanol. Single-layer (s-MoS₂) and double-layer (d-MoS₂) MoS₂ slabs were used to represent the single-layer and multi-layer MoS₂ catalysts, respectively, as adding more layers did not further change the

binding strength of H to the MoS₂ slab (Table S4). Double S vacancy sites on the basal plane were identified as the active site for methanol synthesis from CO₂ on MoS₂ catalysts [25]. We assumed an identical S vacancy concentration on the opposite side of the slab models. The positions of the two opposite S vacancies on s-MoS₂ were determined from a systematic scan, giving two symmetric models with opposite S vacancies on the right (s-MoS₂-R) or left (s-MoS₂-L) side of the active site, which is illustrated in Figure S22. A Mo atom in the active site has a reduced coordination number due to the presence of S vacancies on both sides of the slab. There are no energetically preferred positions of the two opposite S vacancies for d-MoS₂ (Table S5, Figure S23). Following the reaction pathway determined in previous literature, [25,59] we compare the reaction profile of methanol synthesis from CO₂ on

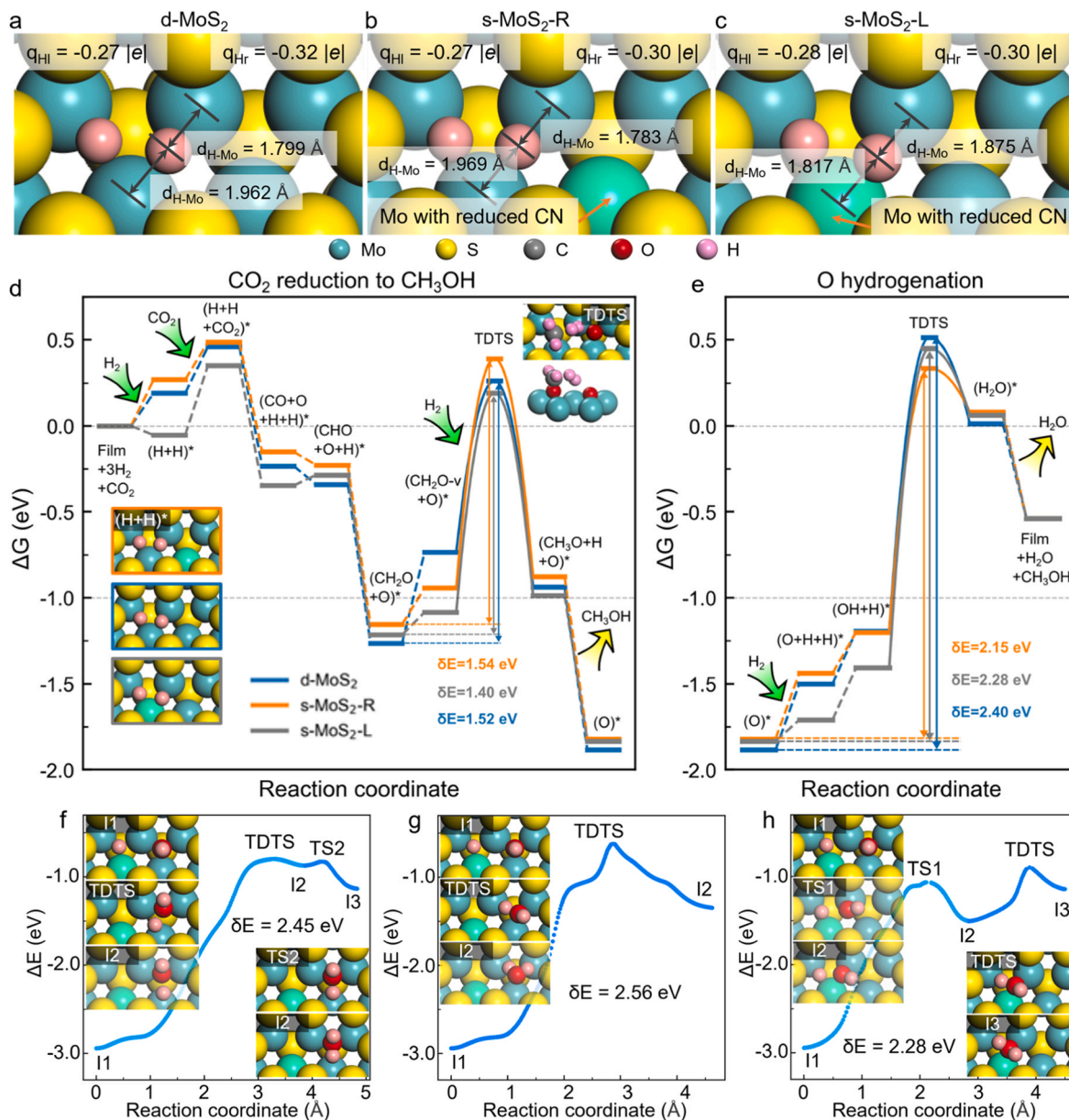


Fig. 7. Theoretical insight into CO₂ hydrogenation over s-MoS₂. Atomic structures of H₂ dissociative adsorption on d-MoS₂ (a), s-MoS₂-R (b), and s-MoS₂-L (c). The Bader charges of the left and right H atoms (q_{Hl} and q_{Hr}) and the H-Mo bond length (d_{H-Mo}) are shown. The Mo atom with reduced coordination number (CN) is highlighted with cyan. Reaction energy profiles of CO₂ reduction to CH₃OH (d) and hydrogenation of O atoms produced through CO₂ dissociation (e). The energetic spans (δE) of the two reactions are shown. Inset: top and perspective views of the TOF-determining transition state (TDTS) of CO₂ reduction to CH₃OH. Elementary steps of different pathways for H₂O formation from OH+H on s-MoS₂-L (f-h). (f) H migrates to Mo site closer to OH and then reacts. (g) H migration and reaction in one elementary step. (h) OH migrates to approach H and reacts. The displayed energetic spans (δE) for O hydrogenation are determined by the Gibbs free energy difference between the TOF-determining transition state (TDTS) and TOF-determining intermediate. Atomic structures of intermediates (I) and transition states (TS) are shown.

monolayer and multilayer MoS₂ (Fig. 7). Other possible pathways (*HCOO or *COOH pathways) are not displayed due to higher activation energies than CO₂ dissociation, as shown in Figure S24. The higher hydrogenation activity of monolayer MoS₂ can already be seen from its interaction with H₂ molecules. Namely, stronger interaction of H atoms with low-coordinated Mo atoms in s-MoS₂-L structure facilitates H₂ activation by making it exothermic by $\Delta G = -0.05$ eV (Figs. 7a–7c). For analysis of methanol synthesis kinetics, we apply the energetic span model to compare the reaction rate on three considered MoS₂ models [60]. The turnover frequencies (TOF) of the reactions are determined by the Gibbs free energy differences between the TOF-determining transition states (TDTS) and the TOF-determining intermediates (TDI), which are identified from the established reaction pathway. TDTS for CO₂ reduction corresponds to the attachment of H₂ molecule on CH₃O* to form CH₃O*+H* (Fig. 7d). The stabilization of this TDTS on s-MoS₂-L decreases the energetic span of CO₂ hydrogenation to 1.40 eV from 1.52 eV on multilayer MoS₂. However, the slowest process during CO₂ reduction to methanol on MoS₂ is not the conversion of CO₂ molecules, but the reduction of surface O atoms produced upon CO₂ dissociation into water molecules. We explored different pathways for H₂O formation from OH+H to identify the TDTS for O hydrogenation, whose structure on monolayer MoS₂ depends on the relative position of intermediates and low-coordinated Mo atoms (Figs. 7f–7h, Figure S25–S26). The H atom can migrate from the left three-fold site to the Mo site closer to OH in one elementary step and react to form H₂O in another elementary step (Figure S25a), which gives an energetic span of 2.47 eV on d-MoS₂. H migration reaction in one elementary step is also possible but with a higher energetic span (2.51 eV) on d-MoS₂ (Figure S25b). OH can migrate from the right three-fold site to the left and react to form water, which gives the lowest energetic span (2.40 eV) for O hydrogenation on d-MoS₂ (Figure S25c). The results indicate that H₂O formation follows the OH migration-reaction pathway on d-MoS₂. The three pathways were also identified on s-MoS₂-R (Figure S26) and s-MoS₂-L (Figs. 7f–7h). The preferred pathway is still OH migration-reaction on s-MoS₂-L, but with a significantly lower energetic span of 2.28 eV, due to the low coordination-number Mo atom at left stabilizing the intermediates (Fig. 7h). However, the intermediates at right are stabilized by the reduced coordination-number Mo atom on s-MoS₂-R, thus changing the preferred reaction pathway of H₂O formation to the H migration-reaction with a small energetic span of 2.15 eV (Figure S26a). In general, monolayer MoS₂ with S vacancies on both sides was calculated to have ~0.25 eV lower activation energy in this process compared to multilayer MoS₂, which rationalizes much higher activity of the former in methanol synthesis (Fig. 7e).

4. Conclusion

In this study, we had successfully fabricated single-layer MoS₂ molecular sheets (s-MoS₂) through instantaneous self-assembling of DA–MoS₄ micelle followed by a simple thermal transformation process. Our presented strategy was exceptionally facile, safe, green, and scalable. The as-obtained single-layer structure of MoS₂ molecular sheets with abundant pores can effectively promote mass transfer and greatly maximize the exposure and accessibility of active Sv. This s-MoS₂ displayed superior performance in CO₂ hydrogenation, furnishing a record STY_{MeOH} of 1.54 g·g_{MoS₂}^{−1}·h^{−1} with 77% methanol selectivity at 36000 mL·g_{cat}^{−1}·h^{−1}, which outperformed other Mo-based catalysts under similar reaction conditions. Furthermore, this s-MoS₂ was durable over 150 h and its single-layer structure remained unchanged, positioning it as a promising catalyst for industrial methanol synthesis. The reaction intermediate and catalytic mechanism was demonstrated by high-pressure *in-situ* DRIFTS. Moreover, the developed protocol could be extended to other transition-metal dichalcogenide such as single-layer WS₂. DFT calculations show that higher catalytic activity of single-layer MoS₂ is due to the low-coordinated in-plane Mo atoms located in the vicinity of Sv on both side of the monolayer. This facile and scalable

strategy for fabrication of single-layer MoS₂ will guide future applications of single-layer transition-metal dichalcogenide in thermal catalytic CO₂ transformations or in other catalytic processes.

CRediT authorship contribution statement

Shenghui Zhou designed and conducted most of the experimental work, data analysis and interpretation, and composed the initial draft of manuscript. Wenrui Ma performed the DFT simulations and drafted the DFT part under Sergey M. Kozlov's supervision, who revised the DFT part. Mohammadreza Kosari assisted with XAS data analysis and reviewed the manuscript. Alvin M. H. Lim assisted with *in situ* DRIFTS test. Hua Chun Zeng conceived the project idea, supervised the research implementation, data analysis, curation and interpretation, and reviewed and revised the manuscript.

Declaration of Competing Interest

The authors declare that they have no known competing financial interests or personal relationships that could have appeared to influence the work reported in this paper.

Data Availability

Data will be made available on request.

Acknowledgements

The authors gratefully acknowledge the financial supports provided by the National University of Singapore and by the National Research Foundation (NRF), Prime Minister's Office, Singapore, under its Campus for Research Excellence and Technological Enterprise (CREATE C4T Programme). This work is also supported by the National University of Singapore (A-0009169–00–00) and Agency for Science, Technology and Research (A*STAR) through Low Carbon Energy Research Finding Initiative (LCERFI01–0033 | U2102d2006). Computational work was performed using resources of the National Supercomputing Centre, Singapore.

Appendix A. Supporting information

Supplementary data associated with this article can be found in the online version at doi:10.1016/j.apcatb.2024.123870.

References

- [1] H. Li, C. Qiu, S. Ren, Q. Dong, S. Zhang, F. Zhou, X. Liang, J. Wang, S. Li, M. Yu, Na⁺-gated water-conducting nanochannels for boosting CO₂ conversion to liquid fuels, *Science* 367 (2020) 667–671.
- [2] S.-T. Bai, G. De Smet, Y. Liao, R. Sun, C. Zhou, M. Beller, B.U. Maes, B.F. Sels, Homogeneous and heterogeneous catalysts for hydrogenation of CO₂ to methanol under mild conditions, *Chem. Soc. Rev.* 50 (2021) 4259–4298.
- [3] S. Das, J. Pérez-Ramírez, J. Gong, N. Dewangan, K. Hidajat, B.C. Gates, S. Kawi, Core-shell structured catalysts for thermocatalytic, photocatalytic, and electrocatalytic conversion of CO₂, *Chem. Soc. Rev.* 49 (2020) 2937–3004.
- [4] C. Tébar-Soler, V. Martin-Diaconescu, L. Simonelli, A. Missyul, V. Perez-Dieste, I. J. Villar-García, J.-B. Brubach, P. Roy, M.L. Haro, J.J. Calvino, Low-oxidation-state Ru sites stabilized in carbon-doped RuO₂ with low-temperature CO₂ activation to yield methane, *Nat. Mater.* (2023) 762–768.
- [5] M. Kosari, K. Lee, C. Wang, S. Rimaz, S. Zhou, E. Hondo, S. Xi, A.M. Seayad, H. C. Zeng, A. Borgna, Optimizing hollow ZSM-5 spheres (hZSM5) morphology and its intrinsic acidity for hydrogenation of CO₂ to DME with copper–aluminum, *Chem. Eng. J.* (2023) 144196.
- [6] W. Li, X. Nie, H. Yang, X. Wang, F. Polo-Garzon, Z. Wu, J. Zhu, J. Wang, Y. Liu, C. Shi, Crystallographic dependence of CO₂ hydrogenation pathways over HCP-Co and FCC-Co catalysts, *Appl. Catal. B* 315 (2022) 121529.
- [7] X. Zhang, S. Han, B. Zhu, G. Zhang, X. Li, Y. Gao, Z. Wu, B. Yang, Y. Liu, W. Baaziz, Reversible loss of core-shell structure for Ni–Au bimetallic nanoparticles during CO₂ hydrogenation, *Nat. Catal.* 3 (2020) 411–417.
- [8] S. Kattel, P.J. Ramírez, J.G. Chen, J.A. Rodríguez, P. Liu, Active sites for CO₂ hydrogenation to methanol on Cu/ZnO catalysts, *Science* 355 (2017) 1296–1299.

- [9] C.F. Shih, T. Zhang, J. Li, C. Bai, Powering the future with liquid sunshine, *Joule* 2 (2018) 1925–1949.
- [10] J. Zhong, X. Yang, Z. Wu, B. Liang, Y. Huang, T. Zhang, State of the art and perspectives in heterogeneous catalysis of CO₂ hydrogenation to methanol, *Chem. Soc. Rev.* 49 (2020) 1385–1413.
- [11] X. Jiang, X. Nie, X. Guo, C. Song, J.G. Chen, Recent advances in carbon dioxide hydrogenation to methanol via heterogeneous catalysis, *Chem. Rev.* 120 (2020) 7984–8034.
- [12] A. Beck, M. Zabilskiy, M.A. Newton, O. Safonova, M.G. Willinger, J.A. van Bokhoven, Following the structure of copper-zinc-alumina across the pressure gap in carbon dioxide hydrogenation, *Nat. Catal.* 4 (2021) 488–497.
- [13] G. Xie, R. Jin, P. Ren, Y. Fang, R. Zhang, Z.-j. Wang, Boosting CO₂ hydrogenation to methanol by adding trace amount of Au into Cu/ZnO catalysts, *Appl. Catal. B* 324 (2023) 122233.
- [14] H. Zhao, R. Yu, S. Ma, K. Xu, Y. Chen, K. Jiang, Y. Fang, C. Zhu, X. Liu, Y. Tang, The role of Cu₁-O₃ species in single-atom Cu/ZrO₂ catalyst for CO₂ hydrogenation, *Nat. Catal.* (2022) 818–831.
- [15] K. Sun, C. Shen, R. Zou, C.-j. Liu, Highly active Pt/In₂O₃-ZrO₂ catalyst for CO₂ hydrogenation to methanol with enhanced CO tolerance: the effects of ZrO₂, *Appl. Catal. B* 320 (2023) 122018.
- [16] T. Pinheiro Araújo, C. Mondelli, M. Agrachev, T. Zou, P.O. Willi, K.M. Engel, R. N. Grass, W.J. Stark, O.V. Safonova, G. Jeschke, Flame-made ternary Pd-In₂O₃-ZrO₂ catalyst with enhanced oxygen vacancy generation for CO₂ hydrogenation to methanol, *Nat. Commun.* 13 (2022) 5610.
- [17] X. Jiang, X. Nie, Y. Gong, C.M. Moran, J. Wang, J. Zhu, H. Chang, X. Guo, K. S. Walton, C. Song, A combined experimental and DFT study of H₂O effect on In₂O₃/ZrO₂ catalyst for CO₂ hydrogenation to methanol, *J. Catal.* 383 (2020) 283–296.
- [18] Z. Feng, C. Tang, P. Zhang, K. Li, G. Li, J. Wang, Z. Feng, C. Li, Asymmetric sites on the ZnZrO_x catalyst for promoting formate formation and transformation in CO₂, *Hydrog. J. Am. Chem. Soc.* 145 (2023) 12663–12672.
- [19] L. Wang, E. Guan, Y. Wang, L. Wang, Z. Gong, Y. Cui, X. Meng, B.C. Gates, F.-S. Xiao, Silica accelerates the selective hydrogenation of CO₂ to methanol on cobalt catalysts, *Nat. Commun.* 11 (2020) 1033.
- [20] S.R. Docherty, O.V. Safonova, C. Copéret, Surface redox dynamics in gold–zinc CO₂ hydrogenation catalysts, *J. Am. Chem. Soc.* 145 (2023) 13526–13530.
- [21] F. Studt, I. Sharafutdinov, F. Abild-Pedersen, C.F. Elkjær, J.S. Hummelshøj, S. Dahl, I. Chorkendorff, J.K. Nørskov, Discovery of a Ni-Ga catalyst for carbon dioxide reduction to methanol, *Nat. Chem.* 6 (2014) 320–324.
- [22] X. Nie, X. Jiang, H. Wang, W. Luo, M.J. Janik, Y. Chen, X. Guo, C. Song, Mechanistic understanding of alloy effect and water promotion for Pd-Cu bimetallic catalysts in CO₂ hydrogenation to methanol, *ACS Catal.* 8 (2018) 4873–4892.
- [23] H. Sugiyama, M. Miyazaki, M. Sasase, M. Kitano, H. Hosono, Room-temperature CO₂ hydrogenation to methanol over air-stable hcp-PdMo intermetallic catalyst, *J. Am. Chem. Soc.* 145 (2023) 9410–9416.
- [24] H. Zhou, Z. Chen, A.V. López, E.D. López, E. Lam, A. Tsoukalou, E. Willinger, D. A. Kuznetsov, D. Mance, A. Kierzkowska, Engineering the Cu/Mo₂CT_x (MXene) interface to drive CO₂ hydrogenation to methanol, *Nat. Catal.* 4 (2021) 860–871.
- [25] J. Hu, L. Yu, J. Deng, Y. Wang, K. Cheng, C. Ma, Q. Zhang, W. Wen, S. Yu, Y. Pan, Sulfur vacancy-rich MoS₂ as a catalyst for the hydrogenation of CO₂ to methanol, *Nat. Catal.* 4 (2021) 242–250.
- [26] F. Studt, Catalysis by unusual vacancies, *Nat. Catal.* 4 (2021) 184–185.
- [27] J. Zheng, L. Huang, C.-H. Cui, Z.-C. Chen, X.-F. Liu, X. Duan, X.-Y. Cao, T.-Z. Yang, H. Zhu, K. Shi, Ambient-pressure synthesis of ethylene glycol catalyzed by C₆₀-buffered Cu/SiO₂, *Science* 376 (2022) 288–292.
- [28] R.I. Walton, Subcritical solvothermal synthesis of condensed inorganic materials, *Chem. Soc. Rev.* 31 (2002) 230–238.
- [29] L. Tang, X. Meng, D. Deng, X. Bao, Confinement catalysis with 2D materials for energy conversion, *Adv. Mater.* 31 (2019) 1901996.
- [30] H. Li, J. Wu, Z. Yin, H. Zhang, Preparation and applications of mechanically exfoliated single-layer and multilayer MoS₂ and WSe₂ nanosheets, *Acc. Chem. Res.* 47 (2014) 1067–1075.
- [31] J. Zheng, K. Lebedev, S. Wu, C. Huang, Tce Ayvali, T.-S. Wu, Y. Li, P.-L. Ho, Y.-L. Soo, A. Kirkland, High loading of transition metal single atoms on chalcogenide catalysts, *J. Am. Chem. Soc.* 143 (2021) 7979–7990.
- [32] B. Sun, L. Ning, H.C. Zeng, Confirmation of Suzuki–Miyaura cross-coupling reaction mechanism through synthetic architecture of nanocatalysts, *J. Am. Chem. Soc.* 142 (2020) 13823–13832.
- [33] G. Zhan, H.C. Zeng, Hydrogen spillover through Matryoshka-type (ZIFs@)_n-1 ZIFs nanocubes, *Nat. Commun.* 9 (2018) 1–12.
- [34] Y.C. Tan, H.C. Zeng, Lewis basicity generated by localised charge imbalance in noble metal nanoparticle-embedded defective metal–organic frameworks, *Nat. Commun.* 9 (1) (2018) 8.
- [35] G. Kresse, J. Hafner, Ab initio molecular-dynamics simulation of the liquid-metal–amorphous-semiconductor transition in germanium, *Phys. Rev. B* 49 (1994) 14251.
- [36] G. Kresse, J. Furthmüller, Efficiency of ab-initio total energy calculations for metals and semiconductors using a plane-wave basis set, *Comput. Mater. Sci.* 6 (1996) 15–50.
- [37] G. Kresse, J. Furthmüller, Efficient iterative schemes for ab initio total-energy calculations using a plane-wave basis set, *Phys. Rev. B* 54 (1996) 11169.
- [38] J.P. Perdew, K. Burke, M. Ernzerhof, Generalized gradient approximation made simple, *Phys. Rev. Lett.* 77 (1996) 3865.
- [39] P.E. Blöchl, Projector augmented-wave method, *Phys. Rev. B* 50 (1994) 17953.
- [40] G. Kresse, D. Joubert, From ultrasoft pseudopotentials to the projector augmented-wave method, *Phys. Rev. B* 59 (1999) 1758.
- [41] S. Grimme, J. Antony, S. Ehrlich, H. Krieg, A consistent and accurate ab initio parametrization of density functional dispersion correction (DFT-D) for the 94 elements H–Pu, *J. Chem. Phys.* 132 (2010) 154104.
- [42] M. Methfessel, A. Paxton, High-precision sampling for Brillouin-zone integration in metals, *Phys. Rev. B* 40 (1989) 3616.
- [43] G. Henkelman, B.P. Uberuaga, H. Jónsson, A climbing image nudged elastic band method for finding saddle points and minimum energy paths, *J. Chem. Phys.* 113 (2000) 9901–9904.
- [44] G. Henkelman, H. Jónsson, A dimer method for finding saddle points on high dimensional potential surfaces using only first derivatives, *J. Chem. Phys.* 111 (1999) 7010–7022.
- [45] H. Shang, T. Wang, W. Zhang, Sulfur vacancy formation at different MoS₂ edges during hydrodesulfurization process: A DFT study, *Chem. Eng. Sci.* 195 (2019) 208–217.
- [46] F. Studt, M. Behrens, E.L. Kunkes, N. Thomas, S. Zander, A. Tarasov, J. Schumann, E. Frei, J.B. Varley, F. Abild-Pedersen, The mechanism of CO and CO₂ hydrogenation to methanol over Cu-based catalysts, *ChemCatChem* 7 (2015) 1105–1111.
- [47] Y. Lei, S. Pakhira, K. Fujisawa, X. Wang, O.O. Iyiola, Ns Perea López, A. Laura Elías, L. Pulickal Rajukumar, C. Zhou, B. Kabis, Low-temperature synthesis of heterostructures of transition metal dichalcogenide alloys (W_xMo_{1–x}S₂) and graphene with superior catalytic performance for hydrogen evolution, *ACS Nano* 11 (2017) 5103–5112.
- [48] K.M. Kwok, S.W.D. Ong, L. Chen, H.C. Zeng, Constrained growth of MoS₂ nanosheets within a mesoporous silica shell and its effects on defect sites and catalyst stability for H₂S decomposition, *ACS Catal.* 8 (2018) 714–724.
- [49] G. Guan, S. Zhang, S. Liu, Y. Cai, M. Low, C.P. Teng, I.Y. Phang, Y. Cheng, K. L. Duei, B.M. Srinivasan, Protein induces layer-by-layer exfoliation of transition metal dichalcogenides, *J. Am. Chem. Soc.* 137 (2015) 6152–6155.
- [50] H. Li, C. Tsai, A.L. Koh, L. Cai, A.W. Contryman, A.H. Frapapan, J. Zhao, H.S. Han, H.C. Manoharan, F. Abild-Pedersen, Activating and optimizing MoS₂ basal planes for hydrogen evolution through the formation of strained sulphur vacancies, *Nat. Mater.* 15 (2016) 48–53.
- [51] C. Lee, H. Yan, L.E. Brus, T.F. Heinz, J. Hone, S. Ryu, Anomalous lattice vibrations of single- and few-layer MoS₂, *ACS Nano* 4 (2010) 2695–2700.
- [52] S. Zhou, H.C. Zeng, Boxlike assemblies of few-layer MoS₂ nanosheets with edge blockage for high-efficiency hydrogenation of CO₂ to methanol, *ACS Catal.* 12 (2022) 9872–9886.
- [53] Y. Huang, Y. Sun, X. Zheng, T. Aoki, B. Pattengale, J. Huang, X. He, W. Bian, S. Younan, N. Williams, Atomically engineering activation sites onto metallic 1T-MoS₂ catalysts for enhanced electrochemical hydrogen evolution, *Nat. Commun.* 10 (2019) 982.
- [54] T. Zeng, X.-D. Wen, G.-S. Wu, Y.-W. Li, H. Jiao, Density functional theory study of CO adsorption on molybdenum sulfide, *J. Phys. Chem. B* 109 (2005) 2846–2854.
- [55] A. Travert, C. Dujardin, F. Maugé, S. Cristol, J.-F. Paul, E. Payen, D. Bougeard, Parallel between infrared characterisation and ab initio calculations of CO adsorption on sulphided Mo catalysts, *Catal. Today* 70 (2001) 255–269.
- [56] T. Weber, J. Muijsers, J. Van Wolput, C. Verhagen, J. Niemantsverdriet, Basic reaction steps in the sulfidation of crystalline MoO₃ to MoS₂, as studied by X-ray photoelectron and infrared emission spectroscopy, *J. Phys. Chem.* 100 (1996) 14144–14150.
- [57] Y. Wang, S. Kattel, W. Gao, K. Li, P. Liu, J.G. Chen, H. Wang, Exploring the ternary interactions in Cu–ZnO–ZrO₂ catalysts for efficient CO₂ hydrogenation to methanol, *Nat. Commun.* 10 (2019) 1–10.
- [58] P. Uvdal, M. Weldon, C. Friend, Adsorbate symmetry and Fermi resonances of methoxide adsorbed on Mo (110) as studied by surface infrared spectroscopy, *Phys. Rev. B* 50 (1994) 12258.
- [59] S. Zhou, W. Ma, U. Anjum, M. Kosari, S. Xi, S.M. Kozlov, H.C. Zeng, Strained few-layer MoS₂ with atomic copper and selectively exposed in-plane sulfur vacancies for CO₂ hydrogenation to methanol, *Nat. Commun.* 14 (2023) 5872.
- [60] L. Falivene, S.M. Kozlov, L. Cavallo, Constructing bridges between computational tools in heterogeneous and homogeneous catalysis, *ACS Catal.* 8 (2018) 5637–5656.